

PROCEEDINGS OF SPIE

SPIEDigitalLibrary.org/conference-proceedings-of-spie

Experimental detection and discrimination of buried targets using an improved broadband CW electromagnetic induction sensor

Waymond R. Scott

Gregg D. Larson

Charles Ethan Hayes

James H. McClellan

SPIE.

Experimental detection and discrimination of buried targets using an improved broadband CW electromagnetic induction sensor

Waymond R. Scott, Jr.^{*}, Gregg D. Larson[†], Charles Ethan Hayes^{*} and James H McClellan^{*}
^{*}School of Elec. and Comp. Eng., Georgia Institute of Technology, Atlanta, GA, USA 30332-0250
[†]Woodruff School of Mech. Eng., Georgia Institute of Technology, Atlanta, GA, USA 30332-0405

ABSTRACT

Experimental data measured at a field test site with a broadband electromagnetic induction (EMI) sensor are presented. The system is an improved version of the Georgia Tech EMI system developed over the past several years. The system operates over a 300 to one bandwidth and is more sensitive while being more power efficient than earlier systems. Data measured with the system will be presented with an emphasis on features in the data that can be used to separate metallic targets from the soil response and to discriminate between certain classes of metallic targets.

Keywords: Electromagnetic induction, EMI, landmine detection, sensor, testing

1. INTRODUCTION

Simple electromagnetic induction (EMI) sensors are capable of detecting most landmines but they will also detect every buried metal object such as bottle tops, nails, shrapnel, and bullets, resulting in an unacceptably high false alarm rate. This is even more problematic for the detection of low-metal anti-personnel landmines as they are extremely difficult to distinguish from clutter using a simple EMI sensor. However, advanced EMI sensors that use advanced signal processing techniques and either a broad range of frequencies or a broad range of measurement times have been shown to be capable of discriminating between buried landmines and many types of buried metal clutter [1-9].

To demonstrate some of the capabilities of a broadband EMI sensor, experimental results from field testing of an improved version of the Georgia Tech EMI system that has been under development for the past several years are presented. The system has improved accuracy and sensitivity while being more power efficient than earlier systems. The accuracy improvements are obtained by improved shielding while the sensitivity improvements are obtained with improved preamplifiers. A switched-mode power amplifier is used to improve the power efficiency without degrading the performance.

Methods and features that can be used to separate the response of metallic targets from the soil response are presented. These include parameters related to the logarithmic soil model and other parameters related to the phase of the soil response. When a target is present, the shape of the measured response has been shown to be a good feature for discrimination between certain classes of metallic targets; however, this feature is degraded when the soil response is comparable to the target response. Methods for dealing with this mixed response by removing the logarithmic soil model are presented. Data from the field test will be used to demonstrate the viability of these methods.

In this paper, the measurement system, field test site, and test conditions are presented in section 2, the measurement model and spatially-filtered data are presented in section 3, the soil model is presented in section 4, and example responses and features of the data are presented in section 5.

^{*} E-mail: waymond.scott@ece.gatech.edu, Tel: 404-894-3048

[†] E-mail: gregg.larson@me.gatech.edu, Tel: 404-894-6026

2. MEASUREMENT SYSTEM

Data collections were performed at a U. S. Government field site using the cart-based EMI sensor system shown in Fig. 1, with the most recent version of the GT EMI sensor. This sensor has several advancements over previous systems including improved shielding of the coils, an improved preamplifier that has been integrated into the sensor head (which lowers the system noise floor), and increased efficiency of the power amplifier. The data acquisition system uses a National Instruments PXI chassis with control and data acquisition hardware capable of generating and acquiring signals simultaneously on multiple channels at rates of up to 200 kSamples/second, a computer, LabVIEW software, and a GPS card, which provides more accurate and consistent measurement timing that can be correlated to external GPS position measurements. An optimized pseudorandom excitation signal composed of 21 discrete frequencies logarithmically spaced between 30 Hz and 90 kHz was generated by the transmitting coil; changes in the generated magnetic field caused by interactions with buried targets was measured using the receiving coil. Data were collected in the time domain for these measurements to allow for investigation of signal processing techniques. The sensor, a single dipole transmit coil and a single quadrupole receive coil, is a prototype for a handheld sensor. The sensor was mounted on a non-metallic platform that isolated the sensor from cart vibrations and was pushed in front of the cart as shown in Fig. 1. Weather conditions prior to the measurements included rain and snow flurries; conditions ranged from 30 to 50 degrees Fahrenheit with snow flurries at times during the measurements but the ground remained firm enough for measurements.

Typical targets for EMI detection, including land mines and various clutter objects, had been previously buried in multiple 30 meter long soil lanes with sufficient separation between adjacent objects to separate the effects attributed to each of the individual buried objects. The standard lane was separated into twenty grid spaces that were each 1.5 m long; grid spaces were labeled alphabetically from one end to the other in each lane. Blank regions were included to allow examination of soil properties without a buried target. Data were collected in each lane with cart speeds of approximately 10, 20, 50, and 100 cm/s; the sensor was positioned at one end of the lane, data acquisition was initiated, data were recorded for five seconds with the sensor stationary, the sensor was pushed the length of the lane at an approximately constant speed while data were recorded, the sensor was stopped at the end of the lane, and data were recorded for approximately five seconds with the sensor stationary before data acquisition was completed. Cart speeds were determined from encoder measurements of the rotation of the rear wheels.



Figure 1. Photograph of the measurement cart.

3. MEASUREMENT MODEL AND SPATIALLY FILTERED DATA

The measured EMI response, $R_m(\omega_k, x_i)$, can be written as:

$$R_m(\omega_k, x_i) = R(\omega_k, x_i) + S(\omega_k, x_i) + G(\omega_k, x_i) \quad (1)$$

where $R(\omega_k, x_i)$ is the target response, $S(\omega_k, x_i)$ is the sensor self response, $G(\omega_k, x_i)$ is the soil response, ω_k are the measurement frequencies, and x_i are the down-track positions at which the measurements are made. $R(\omega_k, x_i)$ will vary relatively quickly as the sensor is scanned over a target. $S(\omega_k, x_i)$ is due to direct coupling between the transmit and receive coils and to eddy currents on the coils, preamplifier, and cables. $S(\omega_k, x_i)$ is relatively large and is very slowly varying if the cables are properly restrained and the sensor is not flexed. The variations in $S(\omega_k, x_i)$ are due mostly to thermal drift and motion of the cables. $G(\omega_k, x_i)$ is the response of the soil and has a component that varies slowly and a component that can vary quickly along the down-track dimension. The slowly varying components of $S(\omega_k, x_i)$ and $G(\omega_k, x_i)$ can be mostly removed by a background-subtraction filter. This can be accomplished by using a zero-mean filter that is convolved with the EMI data. The filtered response has the form

$$R_f(\omega_k, x_i) = F\{R_m(\omega_k, x_i)\} = F\{R(\omega_k, x_i)\} + F\{S(\omega_k, x_i)\} + F\{G(\omega_k, x_i)\} \quad (2)$$

where $F\{\cdot\}$ is the background-subtraction filter that operates on the down-track dimension of the data. The output $F\{S(\omega_k, x_i)\}$ will be very small if the sensor is not flexed and the cables are properly restrained. The filtering will essentially remove the sensor self signature and will lessen the soil response while keeping the target response. Then, the filtered response is

$$R_f(\omega_k, x_i) \approx F\{R(\omega_k, x_i)\} + F\{G(\omega_k, x_i)\} \quad (3)$$

which is the sum of the filtered response of the target and the soil.

In a vehicle based system, the length of the filter and its shape are easy to choose since the shape of the target response and the speed of the sensor is known and relatively constant. A simple filter that consists of one cycle of a sine wave with a length matched to the spatial response of a target can be used [10]. However, for a handheld system, the speed of the scan is unknown and the shape of the target response will not be consistent since the operator may try measurement patterns that home in on the target location. There are several methods that should work in the general situation: for example, a simple high pass filter can be used with the time constant chosen to be reasonable for the usual scan rates. Another possibility is an adaptive filter that adjusts to the scan rates. Wei [11] has developed an adaptive filter that adapts to the scan rates and also encourages the response to have a Discrete Spectrum of Relaxation Frequencies (DSRF) [7-8, 12-16] that has non-negative coefficients. The filter is very promising and appears to be working well, but is computationally intensive. The filter does not guarantee the filtered response will have a non-negative DSRF but does make it more likely. The filter takes N_f frames of data and adaptively makes an optimal response by making a linear combination of the frames. The filter is restricted to be zero mean and to have a unit norm, and the shape of the filter is optimized.

An example graph of the unfiltered data is shown in top graph of Fig. 2 where magnitude of $R_m(\omega_k, x_i)$ is plotted for the 21 frequencies as a function of down-track position. Only the very strong targets at grids are apparent in the measurements before the direct coupling $S(\omega_k, x_i)$ is removed. The center graph is the magnitude of the filtered and shifted response of the 21 frequencies as a function of down-track position when the filter is 75 cm wide. Targets are apparent at almost every grid location with the filter. The bottom graph is a pseudo-color graph of the DSRF as a function of the log of the relaxation frequency and down-track position. The DSRF amplitudes are not normalized and are mapped to a 120 dB color scale. The DSRF is seen to be quite consistent as the sensor passes over the targets. The DSRF signatures are useful in classifying the targets. For example, the targets at grids D, M, and O are the same type of landmine and their DSRF signatures are very similar except for their amplitudes which vary because the targets are buried at different depths. These signatures can also be seen to be different than the signatures of the other targets. A filter that is 40 cm wide is used for the remaining figures in this paper.

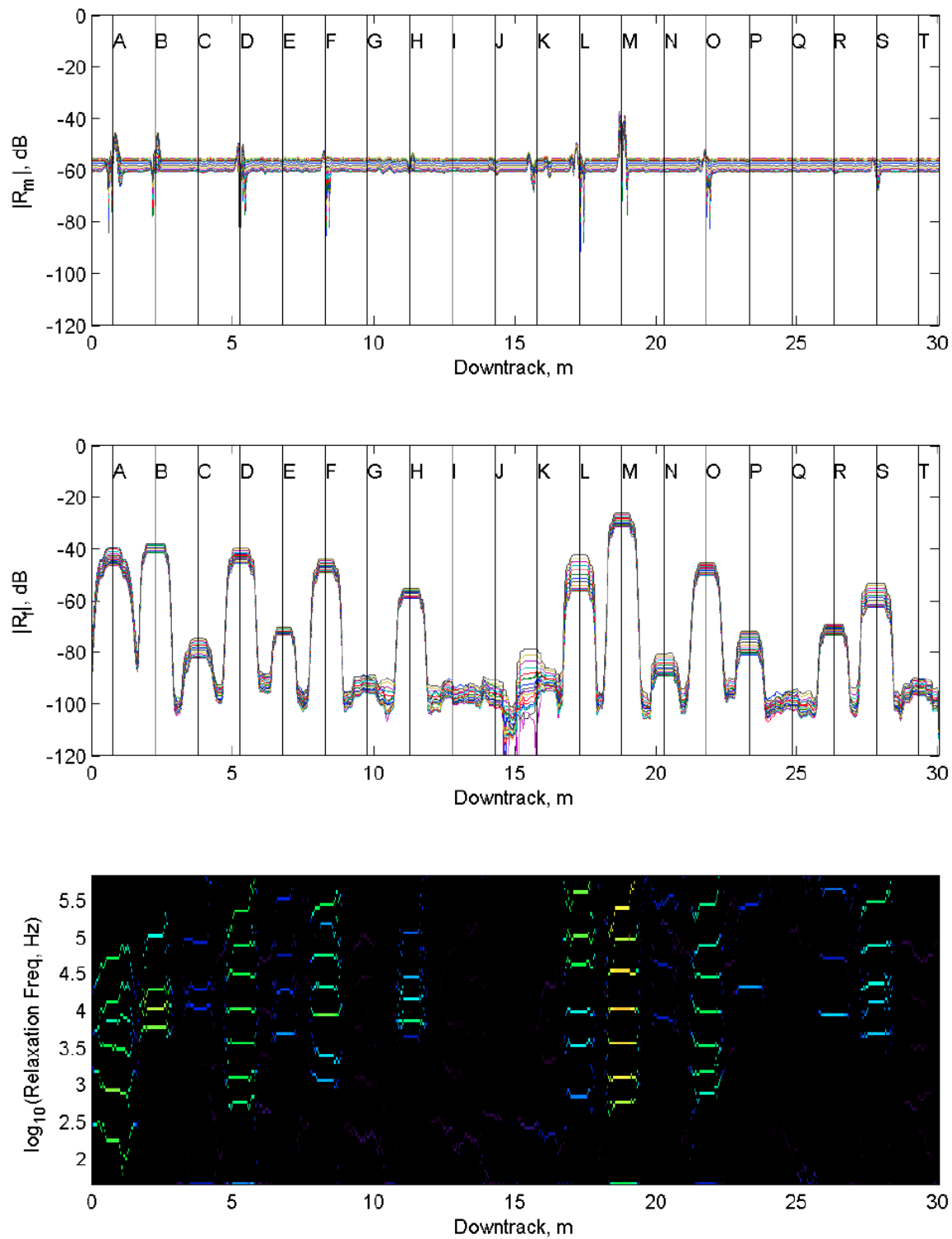


Figure 2. Top: Magnitude of the measured response of the 21 frequencies. Center: Magnitude of the filtered and shifted response of the 21 frequencies with an adaptive filter of length 75 cm. Bottom: pseudo-color graph of the DSRF as a function of the log of the relaxation frequency and down-track position with a 120 dB color scale

4. SOIL MODEL

A commonly used model for the magnetic susceptibility of the soil is one that assumes the particles in the soil have a log-uniform distribution of relaxations over the full measurement bandwidth [17-18]. This model is remarkably simple but has been shown to fit measured data quite well [17, 19-21], has been used as part of the signal processing for many EMI sensors [22-25] and is used in this work. The sensor response from the soil is proportional to the susceptibility in the model:

$$G(\omega_k, x_i) = c_1(x_i) \left[\log\left(\frac{\omega_k}{\omega_M}\right) + \frac{j\pi}{2} \right] + c_2(x_i) \quad (4)$$

which has two free real parameters: $c_1(x_i)$ and $c_2(x_i)$, for each sensor measurement. In this paper we set ω_M to the geometric mean of the measurement frequencies, $\omega_M = \prod_{i=1}^{N_f} \sqrt[N_f]{\omega_i}$, to make $c_2(x_i)$ the mean of the real part of $G(\omega_k, x_i)$. The values of $c_1(x_i)$ and $c_2(x_i)$ depend on the susceptibility of the soil and the coupling of the EMI sensor to the soil which is a strong function of the sensor height above the ground.

The filtered response (3) has one term due to the soil response and this term can be removed by fitting the soil model to the response and keeping the residual. The fitting is done by least squares for each measurement:

$$\dot{c}_1(x_i), \dot{c}_2(x_i) = \underset{\dot{c}_1(x_i), \dot{c}_2(x_i)}{\operatorname{argmin}} \sum_k \left| R_f(\omega_k, x_i) - \dot{c}_1(x_i) \left[\log\left(\frac{\omega_k}{\omega_M}\right) + \frac{j\pi}{2} \right] - \dot{c}_2(x_i) \right|^2 \quad (5)$$

where \dot{c}_1 and \dot{c}_2 are restricted to be real by separating the real and imaginary equations in (5). The residual is the filtered response minus the fit:

$$R_G(\omega_k, x_i) = R_f(\omega_k, x_i) - \dot{c}_1(x_i) \left[\log\left(\frac{\omega_k}{\omega_M}\right) + \frac{j\pi}{2} \right] - \dot{c}_2(x_i). \quad (6)$$

Another way to view operations (5) and (6) together is as a projection onto the subspace that is orthogonal to the soil model subspace spanned by the linear model in (4). Thus,

$$R_G(\omega_k, x_i) = P^\perp \{R_f(\omega_k, x_i)\} = P^\perp \{F[R(\omega_k, x_i)]\} + P^\perp \{F[G(\omega_k, x_i)]\} \quad (7)$$

where $P\{\cdot\}$ is the projection operator onto the soil subspace and $P^\perp\{\cdot\} = (I - P)\{\cdot\}$ is the projection operator onto the orthogonal complement of the soil subspace. Due to the linearity of projection operators, the action of the projection operator can be separated into actions on the target response and soil response parts of (7). If the soil model is a good representation for the soil, the projection onto the orthogonal complement of the soil subspace makes the soil term very small: $P^\perp\{F[G(\omega_k, x_i)]\} \approx 0$. Then,

$$R_G(\omega_k, x_i) \approx P^\perp \{F[R(\omega_k, x_i)]\} \quad (8)$$

which is independent of the soil response. Note that the projection operator will also remove part of the target response. Finally, note that the projection operator can be very efficiently formulated as a simple matrix multiplication based on the linear model in (4).

Graphs of the measured response on a lane are shown in Figs. 4 and 5 to demonstrate the effectiveness of the orthogonal projection operator for the soil model. Grids A through J and M through O on the lane are essentially blank since they contain very deeply buried low-metal landmines. The magnitude of $R_f(\omega_k, x_i)$ as a function of down-track position, x_i , for all 21 frequencies are graphed on the top graph of Fig. 4. The ground response can be lessened by removing the real part of the ground response which is due to the real part of the susceptibility of the soil:

$$R_S(\omega_k, x_i) = R_f(\omega_k, x_i) - \operatorname{mean}_k [Re(R_f(\omega_k, x_i))] = R_f(\omega_k, x_i) - \dot{c}_2(x_i) \quad (9)$$

which is a simple technique for mitigating part of the soil response. Graphs of the magnitude of $R_S(\omega_k, x_i)$ are graphed on the center graph of Fig. 4. Removing the mean lowers the magnitude of the response by about 10 to 20 dB at the locations where the response is dominated by the soil. The ground response can be further lessened by using the orthogonal projection operator. Graphs of the magnitude of $R_G(\omega_k, x_i)$ are graphed on the bottom graph of Fig. 4. This lowers the response by about an additional 20 dB at the locations where the response is dominated by the soil. Notice that the ground response has been greatly reduced in $R_G(\omega_k, x_i)$ relative to $R_f(\omega_k, x_i)$ making the targets easier to find. Note

that no metal targets are evident using the magnitude of $R_f(\omega_k, x_i)$ or $R_S(\omega_k, x_i)$ in Fig. 4; however, metal targets are clearly evident using the magnitude of $R_G(\omega_k, x_i)$.

Several metrics that may be useful in separating the response of soil from a metal target are presented in Fig. 5. The mean of the imaginary part of $R_f(\omega_k, x_i)$ is a common metric

$$M_R(x_i) = \text{mean}_k [Im(R_f(\omega_k, x_i))] \approx \frac{\pi}{2} \dot{c}_1(x_i) \quad (10)$$

and is approximately equal to $\pi\dot{c}_1/2$ and is plotted as the black line on the top graph. The mean of the magnitude $R_G(\omega_k, x_i)$

$$M_G(x_i) = \text{mean}_k [|R_G(\omega_k, x_i)|] \quad (11)$$

is plotted as the dashed-blue line on the top graph. $M_G(x_i)$ is about 20 dB less than $M_R(x_i)$ where the response is dominated by the soil. The strength of $M_G(x_i)$ is a good indication if a metal target is present.

The response angles are graphed as a function of down track position in the bottom two graphs of Fig. 5. These angles are intended to partially represent the shift information that was lost in the measures made above. The angles are defined in Fig. 3 which shows a typical filtered EMI response as an Argand diagram with the imaginary component plotted versus the real component of the EMI response with frequency as a parameter. α_n is the angle to the response at the n^{th} frequency α_M is the angle to the mean of the response:

$$\alpha_M(x_i) = \text{atan2}\left(\frac{\text{mean}_k [Re(R_f(\omega_k, x_i))]}{-\text{mean}_k [Im(R_f(\omega_k, x_i))]} \right) \approx \alpha_G(x_i) = \text{atan2}\left(\frac{\dot{c}_2(x_i)}{-\frac{\pi}{2} \dot{c}_1(x_i)} \right) \quad (12)$$

which is approximately equal to the angle α_G defined by \dot{c}_1 and \dot{c}_2 . The mean of the response is less noisy than the response so these angles may be more useful for weak targets. α_M and α_G are plotted on the center graph of Fig. 5, and the angles α_n are plotted on the bottom figure. For a non-magnetic conductive target, the angles will be between -90 and 0 degrees. For a magnetic target that is not conductive the angles will be approximately 90 degrees. For a magnetic and conductive target the angles will be between -90 and 90 degrees. For a target with a strong eddy current response (conductive), the spread between the angles will be large. These kind of angle measures are commonly used to separating soil and conductive targets. [26-29].

These angles $\alpha_M(x_i)$ are generally about 90 degrees where the response is dominated by the soil. The angle where the response is dominated by the soil will vary according to soil type but will be relatively constant for a given soil type. Here these angles for soil are between about 82 and 88 degrees.

These angles $\alpha_n(x_i)$ are generally tightly grouped at about 90 degrees for all the frequencies where the response is dominated by the soil. The spread of the angles is much greater over metal targets. The value of $\alpha_G(x_i)$, the amplitude of $M_G(x_i)$, and the spread of $\alpha_n(x_i)$ seem to be good discriminators between the soil and the ground response and some combination of these should make a good pre-screener.

From the graphs on Fig. 5, there seems to be targets at the grid locations K, L, maybe M, N, O, P, Q, R, S and T. Grids K, L, M, and N have low-metal AP mines at 3, 3, 4, and 4 inches, respectively. Grids P, Q, R, and S have low-metal AT mines at 1, 1, 2, and 2 inches, respectively. There also seem to be unintentional pieces of metal cutter, between C and D and between D and E.

5. DSRF

The DSRF can be directly computed from $R_f(\omega_k, x_i)$ using the GT non-negative DSRF algorithm [12] or with one of the other algorithms that do not require non-negative coefficients [7,8,13,14]. However, these algorithms will not compute the DSRF directly from $R_G(\omega_k, x_i)$ since the projection operator $P^\perp\{\}$ changes the shapes of the response by removing the ground model from the target response. Fortunately, it is simple to modify the existing DSRF algorithms to allow them to work on the projected data by using the linearity of the orthogonal projection operator. The modification is to apply the projection operator on the columns of the dictionary (matrix Z) as well as the observation vector h of equation (5) in [12]. The first column of Z also needs to be removed. This procedure will work on the other DSRF algorithms as well.

6. EXAMPLE RESPONSES AND FEATURES FROM THE DATA

Example responses and features derived from the data are shown in Figs. 6-9. Each figure contains all the responses from a particular class of targets measured at the field site. Fig. 6 shows responses for 14 occurrences of type A landmines that are buried from 0 to 2 inches deep, Fig. 7 shows response for 19 occurrences of type B landmines that are buried from 0 to 4 inches deep, Fig. 8 shows response for 19 occurrences of type C landmines that are buried from 0 to 5 inches deep, and Fig. 9 shows responses for 54 of the blank grids (regions which were not supposed to have a metallic target buried). Each figure contains 6 separate graphs for a single target type. To make it simple to discuss the graphs, the graphs will be called out by a number 1 - 6 from left to right and from top to bottom, with graph 1 on the top left and graph 6 on the bottom right.

Graph 1 is an Argand diagram of the adaptively filtered response, $R_f(\omega_k, x_i)$, of the target. The down-track position x_i of the response is chosen to be at the strongest response within a ± 15 cm window about the predicted location of the target. The shape and the left-right shift of the responses are usable information for classification of the responses. The landmine targets in these graphs are buried at a range of depths so the responses have varying size with the smallest responses for the deeper landmines. The shape of the response is mostly due to eddy current relaxations of the targets. The shapes are seen to be quite consistent amongst each of the landmine types while being different between types. The weakest responses from the type C landmines have a shape that is different for the stronger responses. This is due to noise and the response from the soil corrupting the response from the landmine. The corruption is not apparent on the stronger responses since it is small relative to the size of the response. The left-right shifts for type A and B landmines are mainly due to the magnetic permeability of these targets: Type A is essentially non-magnetic and Type B is magnetic. The left-right shift for the type C landmines is due the magnetic properties of both the landmine and the soil. For the blank grids, the response is mostly due to the response of the soil. The soil response has a left-right shift with a shape that is mostly a horizontal line on the argand diagrams. The soil response is also plotted on graphs 3 and 4 of Fig. 9. $R_s(\omega_k, x_i)$, which has the left-right shift removed, is plotted in graph 3 and a normalized version is plotted in graph 4. The shape of the soil response is seen to be mostly a horizontal line as predicted by the model (4) in these graphs.

Graph 2 is an Argand diagram of $R_G(\omega_k, x_i)$ which is the adaptively filtered response projected onto the orthogonal complement of the soil subspace. This mostly removes the effects of the soil and it also removes part of the target response so the shapes of the response in graph 2 are different than those in graph 1. The projection also removes the left-right shift due to the permeability of the landmines. Here the shape of the response is almost entirely due to eddy current relaxations of the targets. Like in graph 1, the shapes are seen to be quite consistent amongst each of the landmine types while being different between types. The weakest responses from the type C landmines that are buried very deep have a shape that is different for the stronger responses due noise and other measurement issues. The shape information for these responses is usable information for classification just like that in graph 1, but the shapes in graph 2 should be more independent of the soil and perform better in stronger magnetic soils. Graph 2 is essentially noise for the blank grids in Fig. 9 as expected.

Graphs 4 and 5 of Figs. 6-8 are the DSRF computed from the responses in graphs 1 and 2, respectively. The DSRF's are plotted on a pseudo-gray-scale graph in which the log of the relaxation frequency is plotted on the y axis and the landmine index is plotted on the x-axis and the spectral amplitudes are represented by gray-scale intensity. The landmine indexes are sorted versus the depth of the landmines. The DSRF are computed using the non-negative algorithm [12] for graph 3 and the modified non-negative algorithm described above for graph 4. The modified algorithm was more sensitive than the original algorithm to the range of the values of the relaxation frequencies used in the dictionary. The DSRF is quite consistent for the type A landmines versus index and algorithm. The DSRF is quite consistent for the type B landmines versus index but varies somewhat between graphs 3 and 4. This is not surprising since this landmine has many relaxations making it difficult to compute the DSRF and should not be a problem if one uses only one method in the classification. The DSRF is quite consistent for the type C landmines versus indexes 1-12, but is not for indexes 13-15 due to the weak measured response. The DSRF is also noisier for the modified algorithm; the reason for this is not known but may be less of an issue for other types of DSRF algorithms. The DSRF computed from $R_G(\omega_k, x_i)$ should be more independent of the soil and perform better in stronger magnetic soils.

The measure M_R is plotted as a solid black line and M_G is plotted as a dashed blue line in graph 5. These measures are quite large for the type A and B landmine and are much smaller for the type C landmine. The measure is comparable to the soil for the type C landmines at the deepest depths. These measures are also plotted on Fig. 5 for an entire lane and are good indication of whether the sensor is seeing the soil or a metallic target.

The angle measures are plotted in graph 6 and α_M is plotted as the black filled circles. The angle measures are very different for the landmine targets than for the blank/soil responses and are good indication of whether the sensor is seeing the soil or a metallic target.

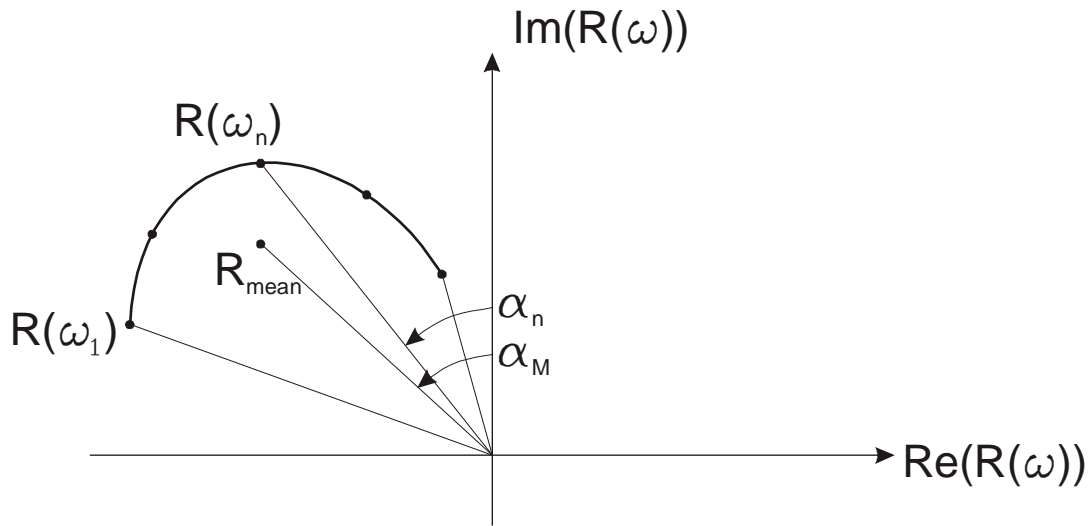


Figure 3. Diagram showing how the angles α_M and α_n are defined.

ACKNOWLEDGMENTS

This work is supported in part by the US Army Night Vision and Electronic Sensors Directorate, Science and Technology Division, Countermine Branch and in part by the U. S. Army Research Office under Contract Number W911NF-11-1-0153.

REFERENCES

1. G. D. Sower and S. P. Cave, "Detection and identification of mines from natural magnetic and electromagnetic resonances," in *Proc. of SPIE* 2496, Orlando, FL, USA, 1995, pp. 1015-1024.
2. C. E. Baum, "Detection and identification of mines from natural magnetic and electromagnetic resonances," in *Detection and identification of visually obscured targets*, C. E. Baum, Ed., ed Philadelphia: Talor and Francis, 1999, pp. 163-218.
3. L. Collins, *et al.*, "An improved Bayesian decision theoretic approach for land mine detection," *Geoscience and Remote Sensing, IEEE Transactions on*, vol. 37, pp. 811-819, 1999.
4. G. Ping, *et al.*, "Classification of landmine-like metal targets using wideband electromagnetic induction," *Geoscience and Remote Sensing, IEEE Transactions on*, vol. 38, pp. 1352-1361, 2000.
5. E. B. Fails, *et al.*, "Performance of a four parameter model for modeling landmine signatures in frequency domain wideband electromagnetic induction detection systems," in *Proc. of the SPIE* 6553, 2007.
6. S. E. Yuksel, *et al.*, "Hierarchical Methods for Landmine Detection with Wideband Electro-Magnetic Induction and Ground Penetrating Radar Multi-Sensor Systems," in *Geoscience and Remote Sensing Symposium, 2008. IGARSS 2008. IEEE International*, 2008, pp. II-177-II-180.
7. Stacy L. Tantum, Waymond R. Scott, Jr., Leslie M. Collins, and Peter A. Torrione, "Target Classification and Identification Using Sparse Model Representations of Frequency-Domain Electromagnetic Induction Sensor Data," *IEEE Transactions on Geoscience and Remote Sensing*, Vol. 51, Issue 5, pp. 2689 - 2706, Sept. 2012. Doi: 10.1109/TGRS.2012.2215876
8. S. Goldberg, T. Glenn, J. Wilson, P. Gader, "Landmine Detection using Two-tapped Joint Orthogonal Matching Pursuits," Proceedings of the SPIE, vol. 8357, Detection and Sensing of Mines, Explosive Objects, and Obscured Targets XVII, April 2012.
9. Wei, M.-H., Scott, W.R., Jr., and McClellan, J.H., "Landmine detection using the discrete spectrum of relaxation frequencies," *2011 IEEE International Geoscience and Remote Sensing Symposium*, pp. 834 – 837, Vancouver, Canada, July 24 - 29, 2011. Doi: 10.1109/IGARSS.2011.6049260
10. Scott, W.R., Jr., "Broadband Array of Electromagnetic Induction Sensors for Detecting Buried Landmines," *2008 IEEE International Geoscience and Remote Sensing Symposium*, Boston, Massachusetts, July 6 - 11, 2008.
11. Wei, M.-H., Scott, W. R., Jr., and McClellan, J. H. "Adaptive Filtering For Nonnegative Discrete Spectrum of Relaxations," submitted to the *IEEE Trans. Geoscience and Remote Sensing Letters*.

12. Wei, M.-H., Scott, W. R., Jr., and McClellan, J. H. "Robust Estimation of the Discrete Spectrum of Relaxations for Electromagnetic Induction Responses," *IEEE Trans. Geoscience and Remote Sensing*, vol. 48, no. 3, pp. 1169–1179, Mar. 2010. Doi: 10.1109/TGRS.2009.2029981
13. Wei, M.-H., McClellan, J. H., and Scott, W. R., Jr., "Estimation of the Discrete Spectrum of Relaxations For Electromagnetic Induction Responses Using p-Regularized Least Squares for $0 \leq p \leq 1$," *IEEE Trans. Geoscience and Remote Sensing Letters*, Vol. 48, No 3, pp 233-237, 2011. Doi: 10.1109/LGRS.2010.2060391
14. Wei, M.-H., McClellan, J.H., and Scott, W.R., Jr., "Application of Lp-Regularized Least Squares For $0 \leq p \leq 1$ in Estimating Discrete Spectrum Models from Sparse Frequency Measurements," *2010 IEEE International Conference on Acoustics, Speech, and Signal Processing (ICASSP)*, pp. 4010 – 4014, March 15 - 19, 2010, Dallas, Texas. Doi: 10.1109/ICASSP.2010.5495769
15. Wei, M.-H., Scott, W.R., Jr., and McClellan, J.H., "Estimation and Application of Discrete Spectrum of Relaxations For Electromagnetic Induction Responses," *2009 IEEE International Geoscience and Remote Sensing Symposium*, pp. 105 – 108, Cape Town, South Africa, July 12 - 17, 2009. Doi: 10.1109/IGARSS.2009.5418012
16. Mu-Hsin Wei, Waymond R. Scott, Jr., James H. McClellan and Gregg D. Larson, "Application of ℓ_p -regularized least squares for $0 \leq p \leq 1$ in estimating discrete spectrum of relaxations for electromagnetic induction responses", Proc. SPIE 7664, 76640F (2010). doi: 10.1117/12.852397
17. Dabas, M., et al., 1992. Magnetic susceptibility and viscosity of soils in weak time varying field. *Geophysical Journal International* 108, 101–109.
18. Das, Y., 2006. Effect of soil electromagnetic properties on metal detectors. *IEEE Transactions on Geoscience and Remote Sensing* 44, 1444–1453.
19. Bailey, R.C., West, G.F., 2005. An instrument for measuring complex magnetic susceptibility of soils. *Proc. SPIE* 5794, pp. 124–134.
20. Mullins, C.E., Tite, M.S., 1973. Magnetic viscosity, quadrature susceptibility, and frequency dependence of susceptibility in single-domain assemblies of magnetite and maghemite. *Journal of Geophysical Research* 78, 804–809.
21. Michael McFadden, and Waymond R. Scott Jr., "Broadband soil susceptibility measurements for EMI applications," *Journal of Applied Geophysics*, Vol. 90, pages 119–125, 2013: DOI: 10.1016/j.jappgeo.2013.01.009
22. Candy, B.H., 1996. Pulse Induction Time Domain Metal Detector.
23. Lhomme, N., et al., 2008. Inversion of frequency domain data collected in a magnetic setting for the detection of UXO. *Proceedings of SPIE* 6953.
24. Pasion, L., et al., 2007. Soil compensation techniques for detection of buried metallic objects using electromagnetic sensors. *Proceedings of SPIE* 6553.
25. Wei, M., et al., 2011. Landmine detection using the discrete spectrum of relaxation frequencies. *IEEE International Geoscience and Remote Sensing Symposium*, pp. 834–837.
26. Claudio Bruschini and Hichem Sahli, "Phase-angle-based EMI object discrimination and analysis of data from a commercial differential two-frequency system", *Proc. SPIE* 4038, Detection and Remediation Technologies for Mines and Minelike Targets V, 1404 (August 22, 2000); doi:10.1117/12.396229.
27. Claudio Bruschini, "A Multidisciplinary Analysis of Frequency Domain Metal Detectors for Humanitarian Demining," Ph.D. Thesis, Applied Sciences of the Vrije Universiteit Brussel. <http://www.eudem.vub.ac.be/files/PhDBruschiniFinalv2Booklet.pdf>
28. Bruschini, C., "On the low-frequency EMI response of coincident loops over a conductive and permeable soil and corresponding background reduction schemes," *IEEE Transactions on Geoscience and Remote Sensing*, Volume: 42 , Issue: 8, 2004. Doi: 10.1109/TGRS.2004.830164
29. McFee, J.E., "Electromagnetic Remote Sensing: Low Frequency Electromagnetics," Defence Research Establishment Suffield, Ralston ALTA (CAN), DRES-SP-124 Jan 1989. <http://cradpdf.rdc-rdc.gc.ca/PDFS/zbc84/p58878.pdf>

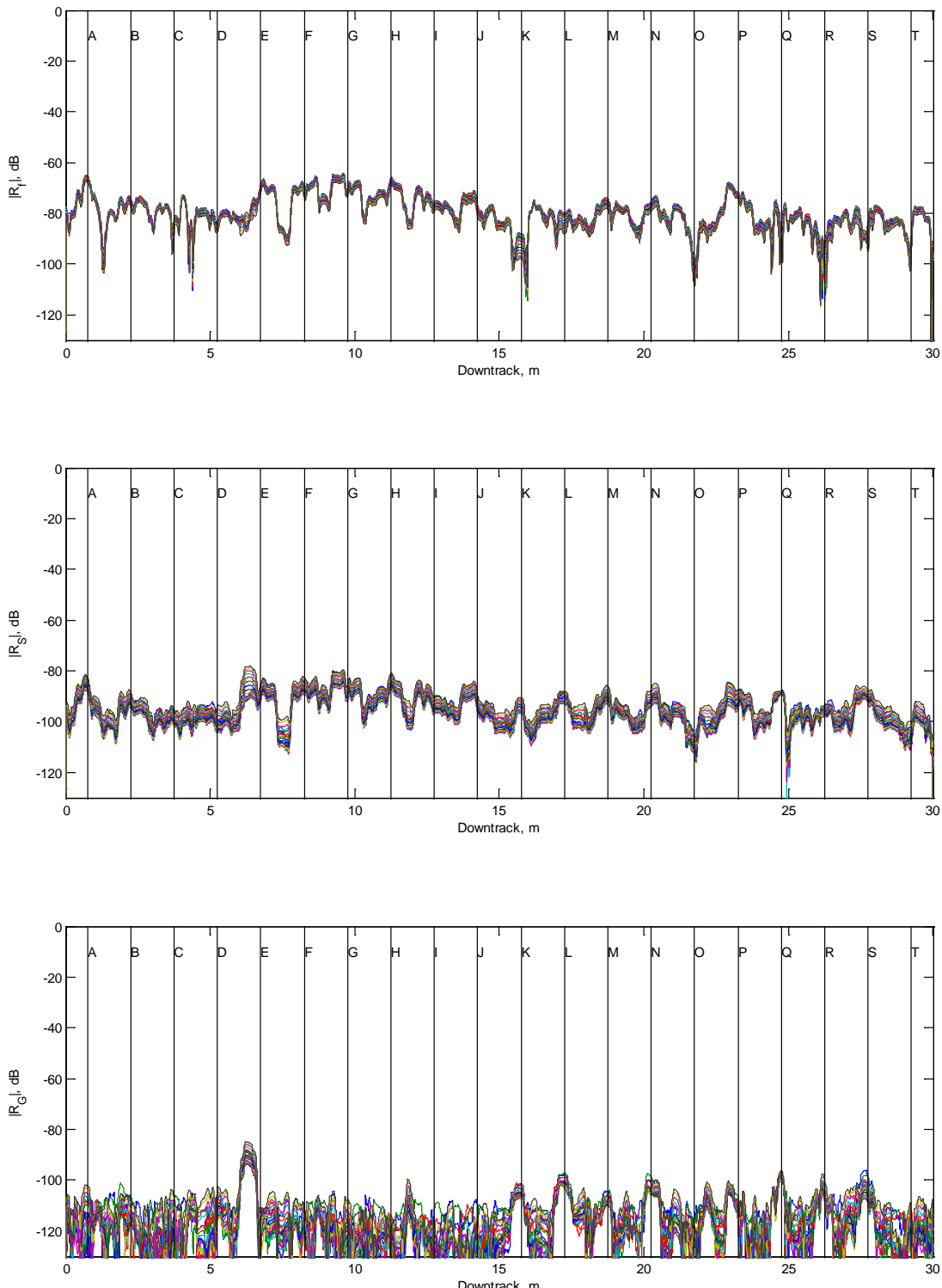


Figure 4: Graphs of R_f , R_S , and R_G for a lane with very weak targets.

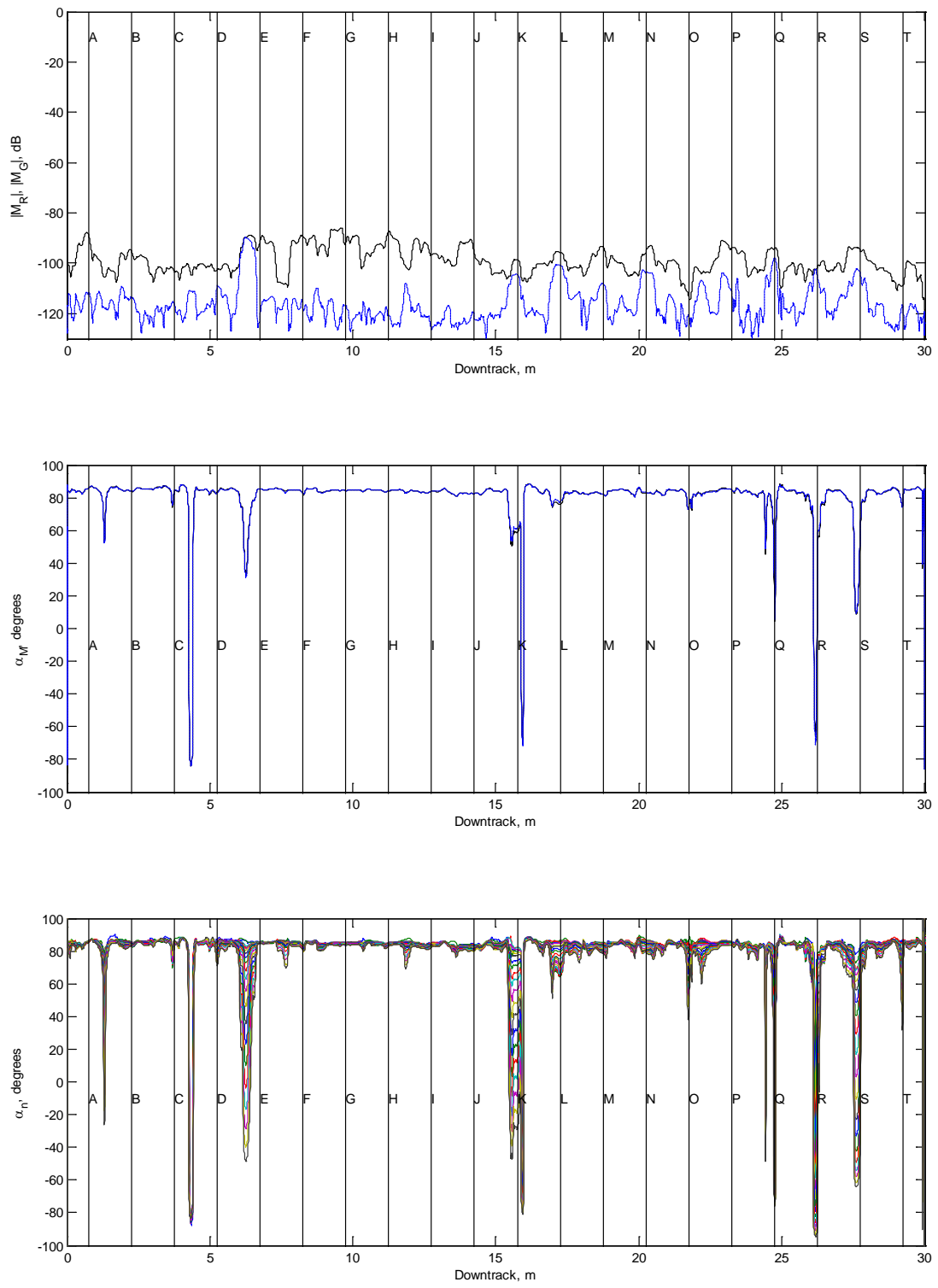


Figure 5: Graphs of angles and amplitudes for a lane with very weak targets..

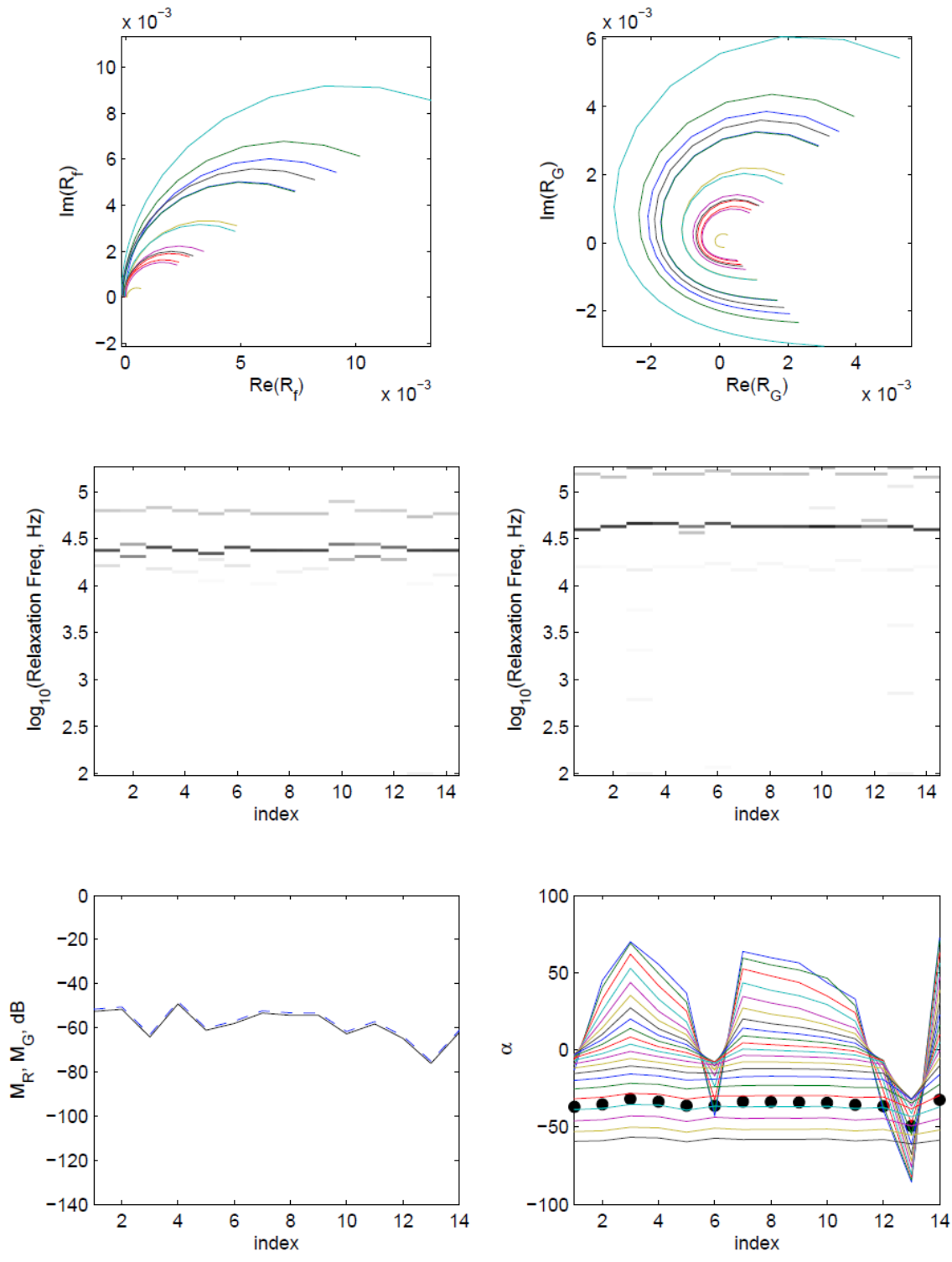


Figure 6: Graphs for the type A landmines.

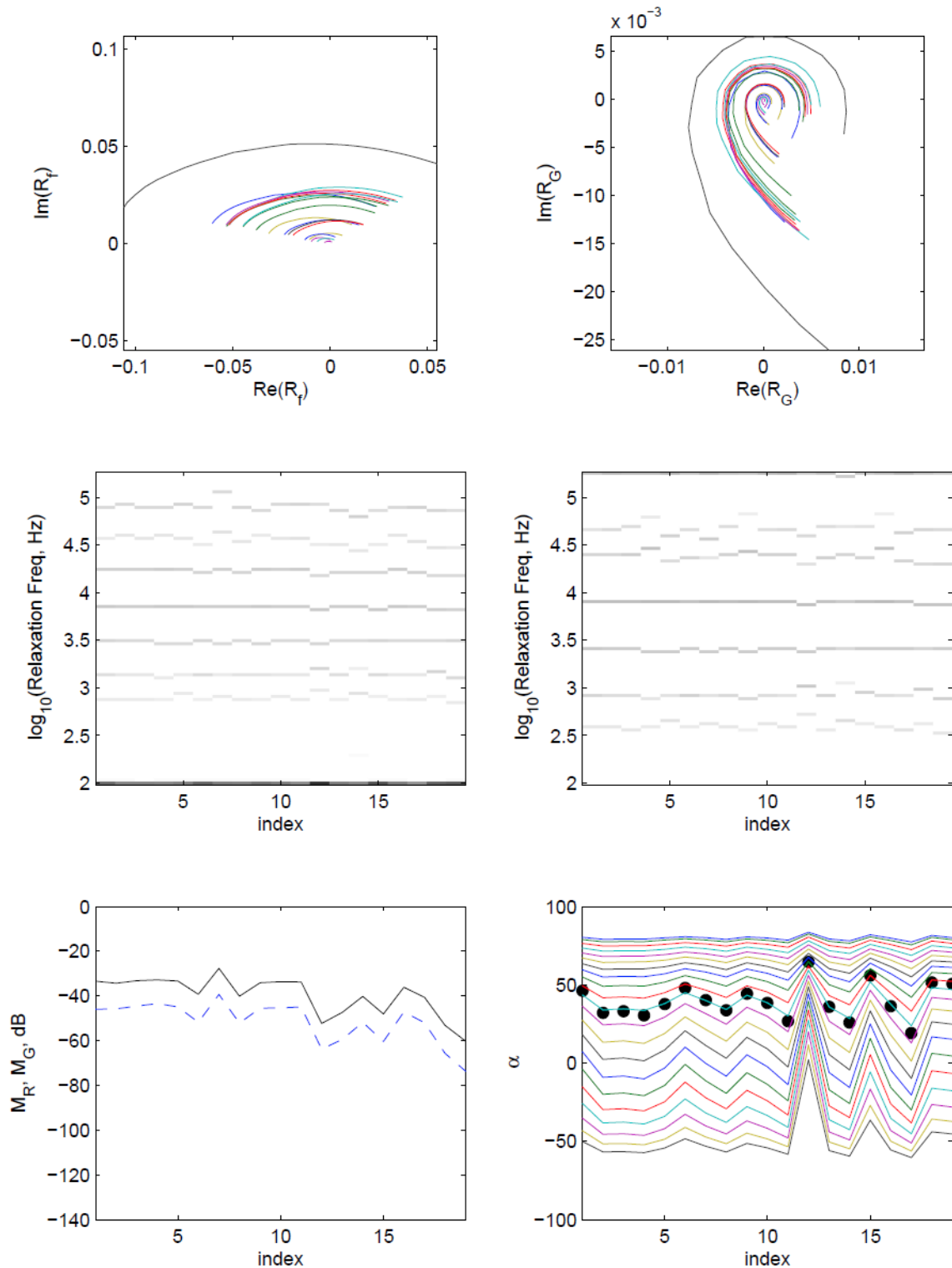


Figure 7: Graphs for the type B landmines.

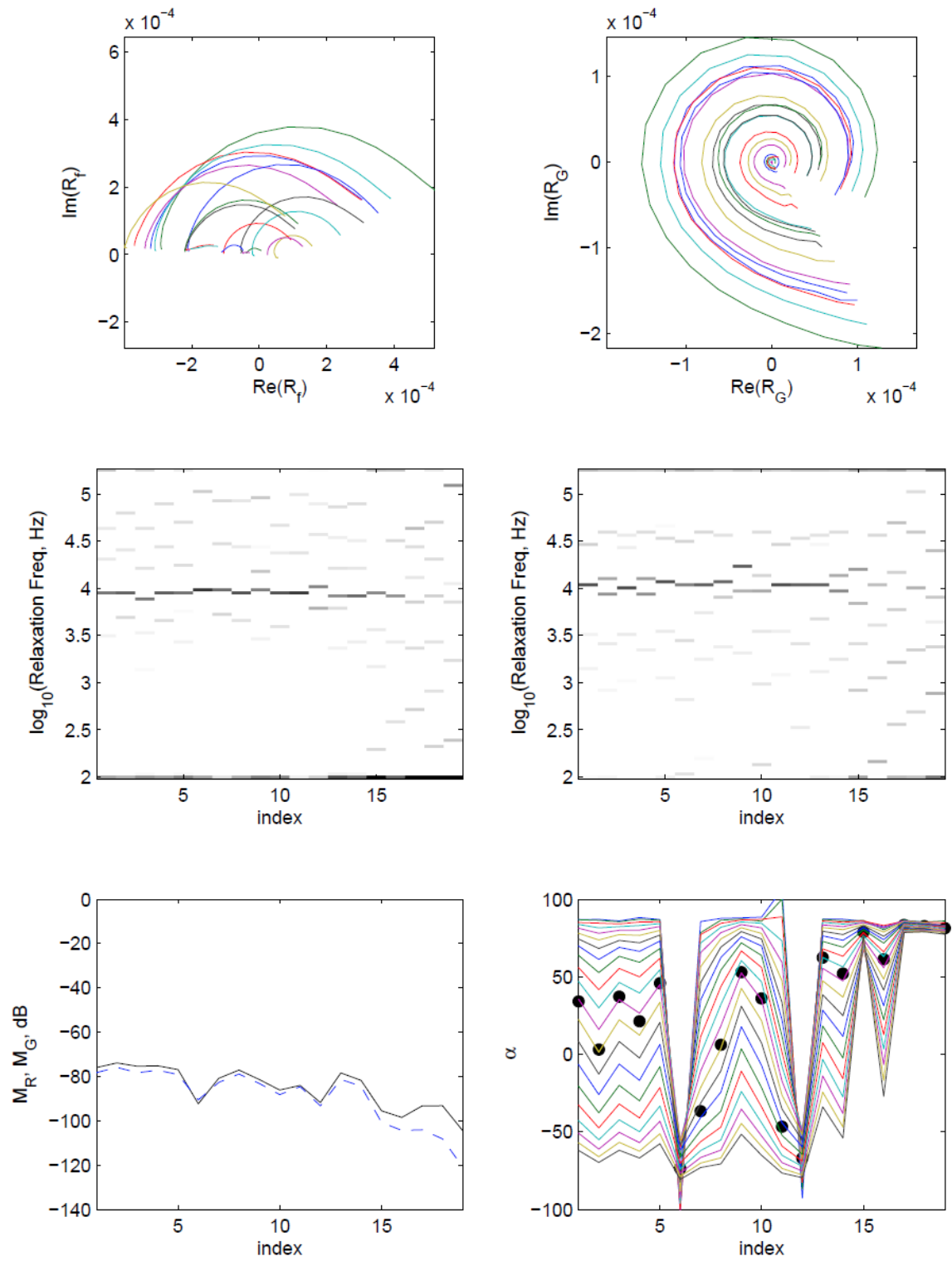


Figure 8: Graphs for the type C landmines.

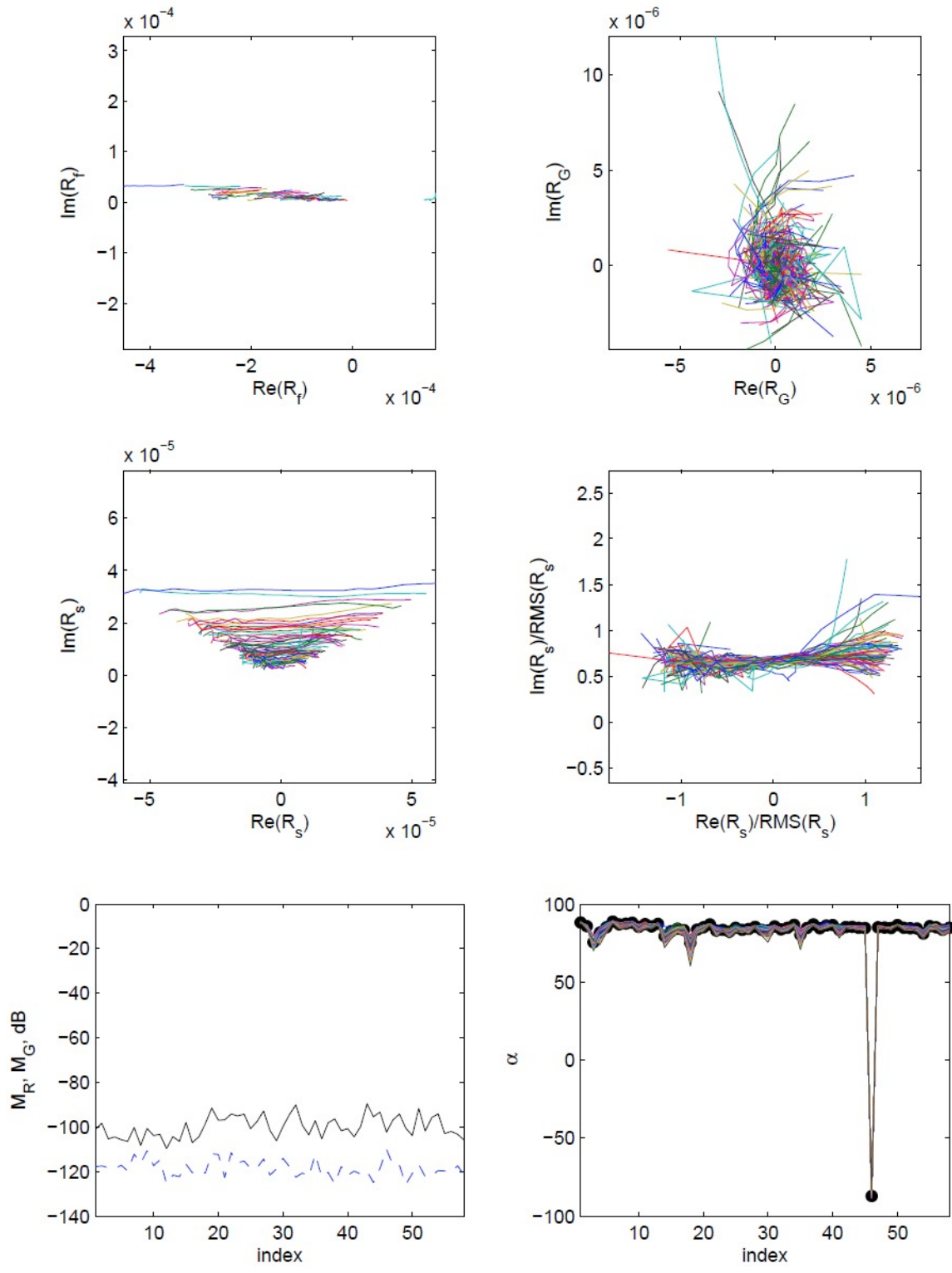


Figure 9: Graphs for the Blank grids.